Revealing grain subdivision initiated nanocrystalline white layer evolution in AISI 52100 steel via hard turning using transmission Kikuchi diffraction

Materials Characterization 234 (2026) 116194

Contents lists available at ScienceDirect

Materials Characterization

journal homepage: www.elsevier.com/locate/matchar

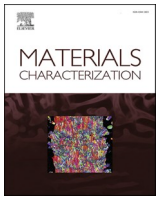

Revealing grain subdivision initiated nanocrystalline white layer evolution in AISI 52100 steel via hard turning using transmission Kikuchi diffraction pattern matching

Sahith Kokkirala [a,*], Seyed B. Hosseini [b], Uta Klement [a]

[a] Industrial and Materials Science, Chalmers University of Technology, SE-412 96 Gothenburg, Sweden
[b] AB SKF, SE-41550 Gothenburg, Sweden

ARTICLE INFO

Keywords:
Hard turning
White layer
Nanocrystalline grains
Tempered martensite
Transmission Kikuchi Diffraction (TKD)
Pattern matching
Dynamic recovery
Grain subdivision

ABSTRACT

During hard turning, tempered martensitic AISI 52100 bearing steel experiences intense thermo-mechanical interactions. These interactions results in the formation of white layers (WLs), characterized by nanocrystalline grains, on the machined surface. The specific cutting conditions, such as feed rate, cutting speed, and tool wear, influence the formation of either mechanically induced (M-WL) or thermally induced white layer (T-WL). The formation of T-WL is primarily driven by continuous dynamic recrystallization associated with the phase transformation mechanisms. However, the underlying grain refinement mechanism for the M-WL resulting in nanocrystalline grains is not fully understood. Nanoscale analysis involving scanning transmission electron microscopy in scanning electron microscopy (STEM-in-SEM) and transmission Kikuchi diffraction (TKD) was used to characterize the microstructural gradients and orientation relationships. In addition, pattern matching analysis combined with TKD has been successfully employed to investigate the evolution of severely deformed nanocrystalline grains. The results reveal that the formation of a M-WL is characterized by nanocrystalline grains on the machined surface, followed by elongated lamellar grains in the underlying material drag region. The presence of these lamellar grains strongly supports the grain subdivision as an initiation mechanism, driven by predominantly severe plastic deformation. The grain subdivision is characterized by the formation of high-angle geometrically necessary boundaries (GNBs) and low-angle incidental dislocation boundaries (IDBs). Furthermore, we attribute the formation of nanocrystalline grains to mechanically assisted triple junction motion, a known dynamic recovery mechanism. These new findings provide crucial insights into understanding the gradient nature of the microstructural evolution of M-WL.

1. Introduction

Hard turning is commonly employed in the finishing process for AISI 52100 tempered martensitic steel to meet the surface integrity requirements and enhance manufacturing flexibility [1–3]. The severe thermo-mechanical interactions between the cutting tool and workpiece material during hard turning often lead to the formation of a thin white layer (WL) on the machined surface [4]. White layers (WLs) are microstructural alterations that appear featureless and white under light optical microscopy due to their nanocrystalline grains [5,6]. Based on the investigation of hard turned AISI 52100 steel, Hosseini et al. [7] identified two distinct WL formation mechanisms, dependent on cutting conditions, i.e., the mechanically induced WL (M-WL) governed by dynamic recovery below the austenitization temperature, and the thermally induced WL (T-WL) driven by dynamic recrystallization above the austenitization temperatures. Transmission electron microscopy (TEM) studies have shown that both the M-WL and T-WL consist of nanocrystalline grains ranging from <10 nm to ~200 nm [4,5,7]. However, subsurface alterations differ significantly between the two types of WLs. The T-WL is typically accompanied by the formation of a dark layer beneath the surface, attributed to high thermal influence. The T-WL exhibits increased surface hardness due to grain refinement and is associated with surface tensile residual stresses, whereas the underlying dark layer results in reduced hardness compared to the bulk material [8]. Several studies have concluded that T-WLs are primarily formed through dynamic recrystallization and phase transformation

* Corresponding author.
E-mail address: sahithk@chalmers.se (S. Kokkirala).

https://doi.org/10.1016/j.matchar.2026.116194
Received 5 August 2025; Received in revised form 1 February 2026; Accepted 22 February 2026
Available online 23 February 2026

mechanisms, driven by large plastic strains combined with significant thermal input from elevated cutting temperatures [6,9,10]. In contrast, the M-WL demonstrates more favourable characteristics, including surface compressive residual stresses, enhanced surface hardness, and the absence of a softened heat-affected dark layer beneath the machined surface [3,8,11]. These characteristics make the M-WL a promising process-induced nanocrystalline surface for demanding engineering applications.

The grain refinement observed in M-WL is primarily attributed to dynamic recovery processes activated by severe plastic deformation (SPD) [5,7,12]. As reported by Zhang et al. [12], during dynamic recovery, martensitic laths undergo reorientation and elongation along the shear direction, while dislocations begin to organize into subgrains structures via the formation of cell boundaries. It has been suggested that grain boundary mobility plays a critical role in determining the minimum achievable grain size during SPD processes such as high-pressure torsion, where larger grains progressively break down through the formation of low-angle grain boundaries (LAGBs) [13]. Interestingly, Yu et al. [14,15] observed a structural evolution comprising lamellar grains and suggested mechanically assisted triple junction motion as a dynamic recovery mechanism facilitating grain refinement in cold-rolled aluminium at high strains. Comparable behaviours have also been reported in severely deformed tantalum at elevated temperatures and in extremely cold-rolled copper [16,17]. These findings provide valuable insights and the motivation to investigate the microstructural evolution of M-WLs formed under extreme conditions, such as hard turning, where the underlying mechanisms of grain refinement resulting in nanocrystalline grains are still not fully understood.

Understanding the formation mechanisms of M-WLs requires detailed post-mortem microstructural analysis. However, this is often constrained by challenges related to specimen preparation and the advanced microscopy techniques needed to resolve highly strained nanocrystalline grains. While transmission electron microscopy (TEM) has been widely used for nanostructure characterization [7], accurately quantifying grain size and grain boundary misorientations over large-area from bright or dark field TEM images remains difficult. Electron backscatter diffraction (EBSD), a commonly employed orientation mapping technique, is effective for materials with grain sizes in the micron range [18], but its spatial resolution, typically limited to ~20 nm, limits its usefulness for nanoscale analysis. Transmission Kikuchi Diffraction (TKD) offers a significant enhancement in spatial resolution, utilizing a thin foil geometry where the diffraction pattern forms at the bottom surface of the sample, resulting in a smaller interaction volume and spatial resolution as fine as 2 nm [19]. However, even with TKD analysis, the indexing of heavily deformed steels with nanocrystalline grains (WLs) remains a challenge due to factors such as sample thickness and curtaining effects introduced during focused ion beam (FIB) sample preparation [20–22]. Moreover, the high dislocation density in severely deformed regions often causes blurred or overlapping diffraction patterns, which significantly degrades TKD band contrast quality and results in low indexing rates [23]. To overcome this issue, pattern matching indexing is developed complementary to Hough-based indexing, which compares the experimentally stored Kikuchi patterns with the dynamically simulated patterns, offering benefits by improving the poorly indexed patterns using the image correlation method [24–26]. The integration of the TKD technique with pattern matching indexing has been shown to enhance the accuracy and precision of crystallographic orientation, as demonstrated in the studies of dental enamel [27].

The primary objective of this study is to investigate the microstructural evolution of M-WL in AISI 52100 hardened steel, from the machined surface down to the unaffected region, to understand the gradient nature of the microstructure. This is systematically compared with the well-established T-WL formed through dynamic recrystallization. TKD pattern matching is employed to provide insights into the formation of nanocrystalline grains within WLs and to demonstrate its applicability in characterizing highly strained tempered martensitic microstructures.

2. Materials and methods

2.1. Material and hard turning process

The material investigated in this study was AISI 52100 steel, a high-carbon, chromium-containing alloy. Its nominal chemical composition, in weight percent (wt%), is 0.95% C, 1.42% Cr, 0.32% Mn, 0.26% Si, 0.001% S, and 0.009% P. To achieve the desired final microstructure of tempered martensite, standard through-hardening heat treatments were applied to the as-received spheroidize-annealed samples. This involved austenitizing the material at 840 °C, followed by oil quenching, and then tempering at 240 °C until the retained austenite (RA) content was less than 2%. The longitudinal hard turning tests were carried out on a MONFORTS RNC 500 SingleTurn high-precision machine. The cutting tools used were TiAlBN-coated polycrystalline cubic boron nitride (PCBN) inserts, specifically BNC 2125 (DNGA 1506 S01035), featuring a 2 mm nose radius and a 35° tool chamfer angle. All machining operations were conducted using cutting fluids. For consistency across all tests, the depth of cut was set at 0.2 mm, and the coolant pressure was maintained at 150 bar. From prior experimental findings [3,11,28], we conducted four tests using both fresh inserts and worn inserts with a tool flank wear (*VB*) of ~0.2 mm (Table 1). We specifically chose the process parameters to create distinct types of white layers, i.e.: M-WLs and T-WLs.

2.2. Sample preparation

To study the white layers on the hard turned surface using light optical microscope (LOM) and scanning electron microscope (SEM), the samples were cut from the hard turned specimens, and standard metallography protocols were performed including mounting, grinding, and polishing using diamond suspension (9, 3, and 1 μm). The final polished samples were etched with 2% Nital. Additionally, to study the orientation of the bulk material using EBSD analysis, the sample was polished using 0.05 μm colloidal silica for 4 min after the 1 μm diamond suspension step. For the scanning transmission electron microscope in scanning electron microscope (STEM-in-SEM) imaging and TKD analysis, a thin lamella was prepared using a site-specific focused ion beam (FIB) lift-out technique in the dual-beam FEI Versa 3D equipment as shown in Fig. 1. To protect the machined surface, a platinum (Pt) layer was deposited using electron beam (at 2 kV, 4 nA) followed by the ion beam Pt deposition (at 30 kV, 100 pA) (Fig. 1b). The FIB milling was performed at 30 kV with decreasing currents ranging from 15 nA to 50 pA to reduce the beam damage on the sample. After the undercut sectioning (Fig. 1d), the lamella was then lifted out using a micromanipulator and welded to a copper (Cu) half grid using ion beam deposited Pt to perform thinning of the lamella (Fig. 1e). The final polishing steps were performed at 5 kV, 48 pA and 2 kV, 27 pA to achieve electron transparency and to minimize the FIB induced amorphous layer (Fig. 1f). The thickness of the lamella was varying between 80 and 100 nm. The thickness is an important consideration for TKD, with a significant impact on both pattern quality and spatial resolution.

Table 1
Hard turning process parameters used in this study.

Inserts	Cutting speed (V_c)	Feed rate (f)
Fresh, worn (~ 0.2 mm)	60 m/min	0,05 mm/rev
Fresh, worn (~ 0.2 mm)	110 m/min	0,2 mm/rev

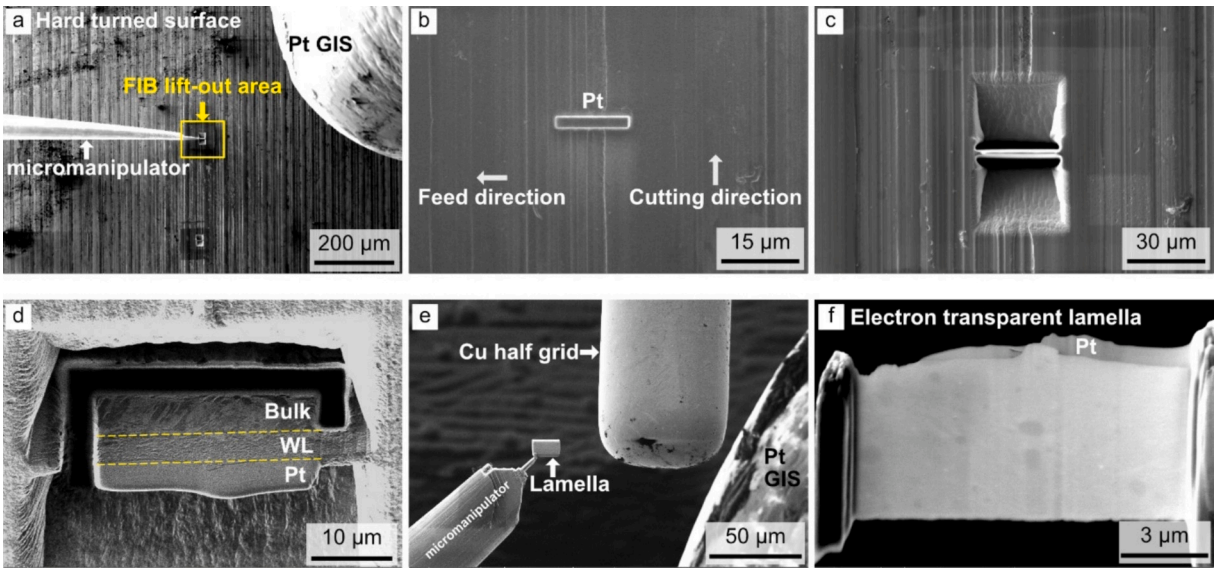

Fig. 1. Sample preparation using FIB technique for STEM-in-SEM and TKD analysis. (a) Overview of the selected area of interest (AOI) on the hard turned surface. (b) Pt deposited on the AOI parallel to the feed direction. (c) Milling performed surrounding the AOI for the lift-out. (d) White layer (WL) exhibiting a refined microstructure observed beneath the Pt deposition. (e) Extraction of the lamella using a micromanipulator and subsequent welding of the lamella to a Cu half-grid. (f) Final electron-transparent lamella obtained after thinning and polishing.

2.3. Microscopy analysis

To examine the microstructural features of the white layers, samples were prepared via mechanical polishing and subsequent Nital etching. The mounted, polished and etched cross-section samples were investigated using a Zeiss Axioscope 7 LOM. Further, the prepared samples were then investigated using a Zeiss Gemini 450 SEM equipped with a field emission gun (FEG). Secondary electron (SE) imaging was performed at an accelerating voltage of 3 kV, a current of 500 pA, and a working distance ranging from 5 to 6 mm. EBSD data on the bulk material was acquired using the same Zeiss Gemini 450 SEM, which was equipped with an Oxford Symmetry detector. The acquisition was performed at an accelerating voltage of 20 kV, probe current of 12 nA, and 1000× magnification with a step size of 150 nm. AztecCrystal 3.3 was used to process and visualize the acquired EBSD maps, with a single iteration of the AutoClean function applied for data cleaning. To gain a deeper understanding of the nanocrystalline structure within the white layers, the thin lamellae prepared using the focused ion beam (FIB) technique were subsequently analysed using the annular STEM (aSTEM) detector built into the Zeiss Gemini 450 SEM (STEM-in-SEM). The STEM-in-SEM bright field (BF) imaging was performed at a probe current of 500 pA, an accelerating voltage of 30 kV, and a working distance between 3.8 mm and 4 mm (See Fig. 2.). Prior to the analysis, all samples (both mechanically polished and FIB lamellae) underwent a 5-min plasma cleaning (Evactron) at 50 W power within the SEM chamber to remove hydrocarbon contamination.

2.4. TKD and pattern matching analysis

The off-axis TKD acquisition was performed on the thinnest sections of the lamella using the Zeiss Gemini 450 SEM equipped with an Oxford Symmetry detector. Data was acquired using an accelerating voltage of 30 kV, a beam current of 5 nA, and step sizes of 5 nm and 10 nm. For optimal signal acquisition, the sample was placed in a 20° pre-tilted holder, and the SEM stage was further tilted to −20°, which aligned the sample horizontally within the chamber. The sample was placed above the EBSD detector phosphor screen with a working distance of 4–5 mm. Data acquisition was carried out using the Aztec 6.2 software (Oxford Instruments Nanoanalysis). To prevent the beam/sample drift, a common challenge during high-resolution acquisition (step sizes of 5 nm or less), drift correction was applied. Additionally, shadow correction was used to remove the shadowing effect caused by thicker outer sections of the lamella on the TKD patterns. The EBSD detector was configured to “Speed 2” mode with a gain 2 setting for pattern acquisition. Each TKD pattern was analysed using a standard Hough-transform approach to detect Kikuchi bands, and all measurement

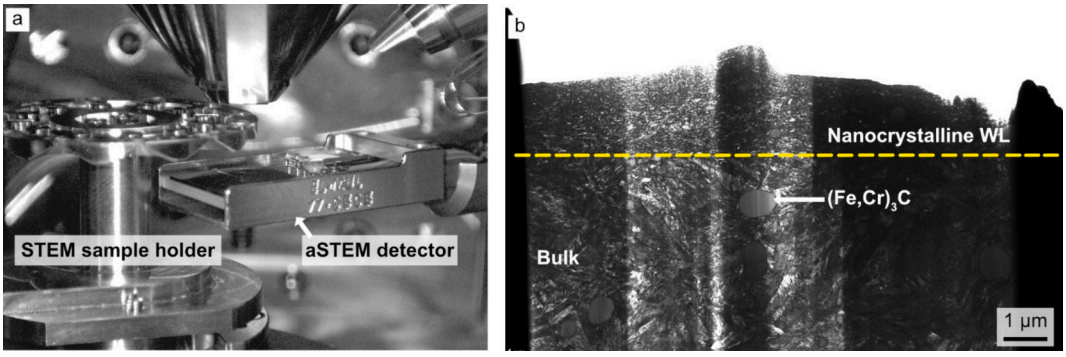

Fig. 2. STEM-in-SEM analysis. (a) In-chamber camera image showing the standard set-up. (b) BF image of the FIB-prepared sample showing the nanocrystalline WL and a µm-sized nearly spherical $(Fe,Cr)_3C$ cementite precipitate.

patterns were stored for subsequent analysis.

The stored TKD patterns and data were exported to .h5oina format and processed using Oxford Instruments AZtecCrystal 3.3 software's "MapSweeper" pattern matching technique. This method compares experimentally stored TKD patterns to a dynamically simulated pattern database, generated from all possible crystal orientations [24,27]. The normalized cross-correlation coefficient (R), ranging from 0 to 1, quantifies the experimental and simulated pattern similarity and the orientation with the highest R-value is chosen as the best index. Since any two arbitrary images result in an R value >0, a minimum R threshold is essential and to ensure reliability, a minimum R-threshold of 0.25 was applied. From crystallography open database (.cif) files, master pattern simulation files for BCC iron and Fe_3C cementite precipitates were developed. Dynamic simulations were performed at 30 kV beam energy (matching TKD acquisition conditions) with a minimum intensity of 16% (39 reflectors), minimum lattice spacing of 0.6 Å, Debye-Waller factor of 0.5, 1001 × 1001 pixel size, and a relative filter radius of 5%. A 2D Gaussian window function was applied to both simulated pattern templates and experimental TKD patterns to minimize shadowing effects, a common issue in the off-axis TKD. The pattern center and detector distance were optimized by calibrating the projection parameters at 9 points that were previously indexed via Hough transform. The optimized values were subsequently applied across the full TKD pattern matching dataset. The analysis employed three modes: indexing, refinement, and repair. The indexing mode reindexed previously unassigned (zero-solution) pixels using dynamic template matching, with a 2° orientation spacing and 78 × 64 pixels (2 × 2 binning) resolution. In refinement mode, the stored TKD patterns are binned to a similar pixel resolution of 78 × 64 pixel (2 × 2 binning). The repair mode replaced zero solutions if band contrast exceeded 10 and validated/replaced small clusters of less than 5 pixels based on neighbouring measurements. Orientation measurements were accepted only if $R >$ 0.25, ensuring that unreliable indexing resulted in zero solutions rather than interpolated data. Finally, the reindexed TKD pattern matching maps were processed and plotted using AztecCrystal 3.3, with data cleaned via a single AutoClean iteration. Fig. 3 illustrates the effectiveness of a pattern matching technique in enhancing the indexing rate of deformed nanocrystalline grains, with an improvement from 18% to 71%. The black region corresponds to zero solutions.

3. Results

3.1. Initial microstructure

Fig. 4a shows a secondary electron image (SE-SEM) of the initial microstructure of AISI 52100 steel, taken after etching with 2% Nital. This image clearly reveals a tempered martensitic microstructure. The microstructure primarily consists of nano-sized tempered cementite dispersed within lath or plate martensite, accompanied by μm-sized nearly spherical $(Fe, Cr)_3C$ cementite precipitates and less than 2% retained austenite (RA) content. The final hardness of the tempered microstructure ranges from 58 to 60 HRC. The EBSD inverse pole figure (IPF) orientation map along the x-axis, shown in Fig. 4b, indicates a random crystallographic orientation distribution. The weighted-average grain size of martensite blocks with >10° high-angle grain boundaries (HAGBs) is measured to be approximately 1.9 ± 0.6 μm. The reconstructed prior austenite grain size (PAGS), as measured from EBSD data in Fig. 4c, has an average value of 10.1 ± 2.3 μm. Quantitative EBSD analysis further indicates that the volume fraction of μm-sized $(Fe, Cr)_3C$ cementite precipitates is approximately 3.6%. These precipitates exhibit an average size of 0.8 ± 0.2 μm and an average aspect ratio of 1.5 ± 0.4, confirming their near-spherical morphology.

3.2. Nanocrystalline white layers

The cross-sectional LOM images of samples generated after hard turning, where either mechanically or thermally induced white layers were formed along the feed direction are shown in Figs. 5a-d. One distinguishing feature between the M-WL and T-WL is the presence of a dark layer observed beneath the T-WL using LOM. The SE-SEM images of the machined surfaces, along the feed direction are shown in Figs. 5e-h. At a cutting speed (*Vc*) of 60 m/min and a feed rate (*f*) of 0.05 mm/rev, machining with a fresh insert resulted in a thinner M-WL (F), as shown in Fig. 5a,e, compared to machining with a worn insert under the same conditions, which resulted in a thicker M-WL (W) (Fig. 5b,f). When the cutting parameters were increased to *Vc*: 110 m/min and *f*: 0.2 mm/rev, the fresh insert generated a discontinuous T-WL (F) (Fig. 5c,g), while the worn insert resulted in a more pronounced T-WL (W) (Fig. 5d,h). The microstructural change within this dark layer is clearly visible and thicker when machining with a worn insert (Fig. 5d,h) as compared to when using a fresh insert (Fig. 5c,g). This dark layer indicates a significant temperature gradient from the machined surface into the bulk

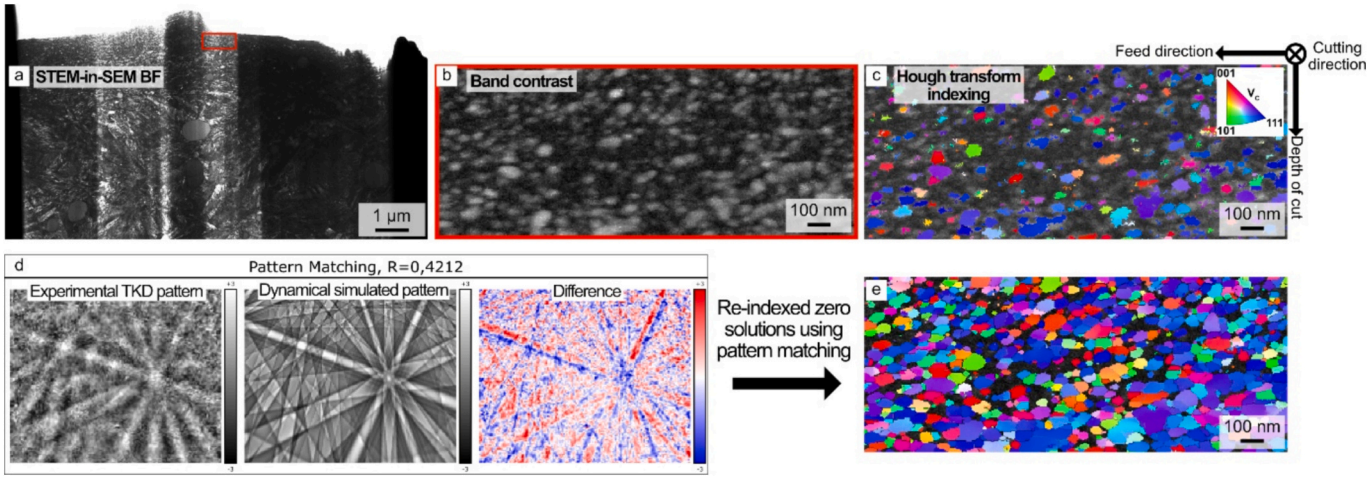

Fig. 3. Example of TKD pattern matching analysis. (a) STEM-in-SEM BF image of the electron transparent lamella with red box representing the selected nanocrystalline region for TKD. (b) The TKD band contrast image of the nanocrystalline grains at the machined surface. (c) Inverse pole figure (IPF) orientation map overlaid on band contrast image, obtained using Hough transform indexing with a hit rate of 18%. (d) Comparing the normalized cross-correlation coefficient (R) between experimentally stored pattern and the dynamically simulated pattern. (e) IPF orientation map generated using the pattern matching technique with an indexing rate of 71%. (For interpretation of the references to colour in this figure legend, the reader is referred to the web version of this article.)

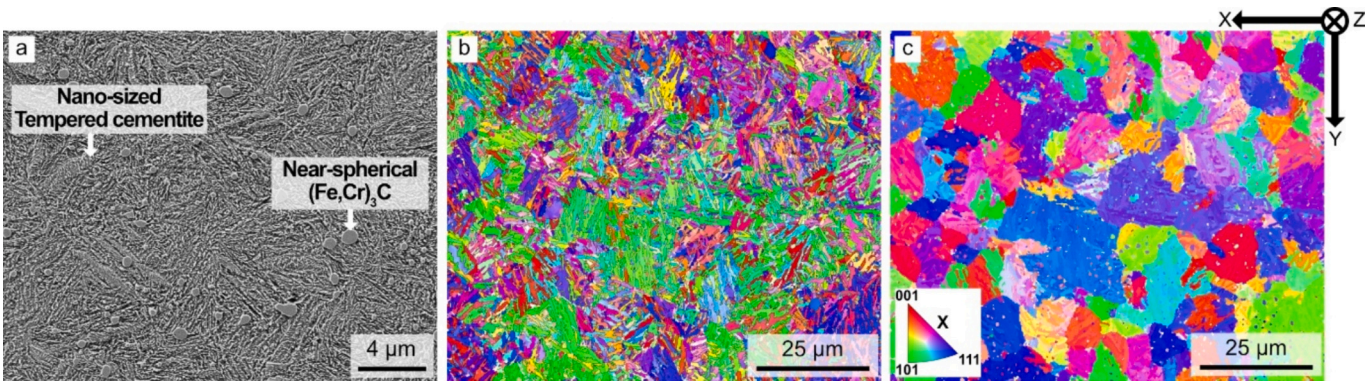

Fig. 4. Initial microstructure of the AISI 52100 tempered martensitic steel. (a) SE-SEM image consisting of nano-sized tempered cementite and near-spherical (Fe, Cr)$_3$C cementite precipitates. (b) EBSD inverse pole figure (IPF) orientation map. (c) Reconstructed prior austenite grains.

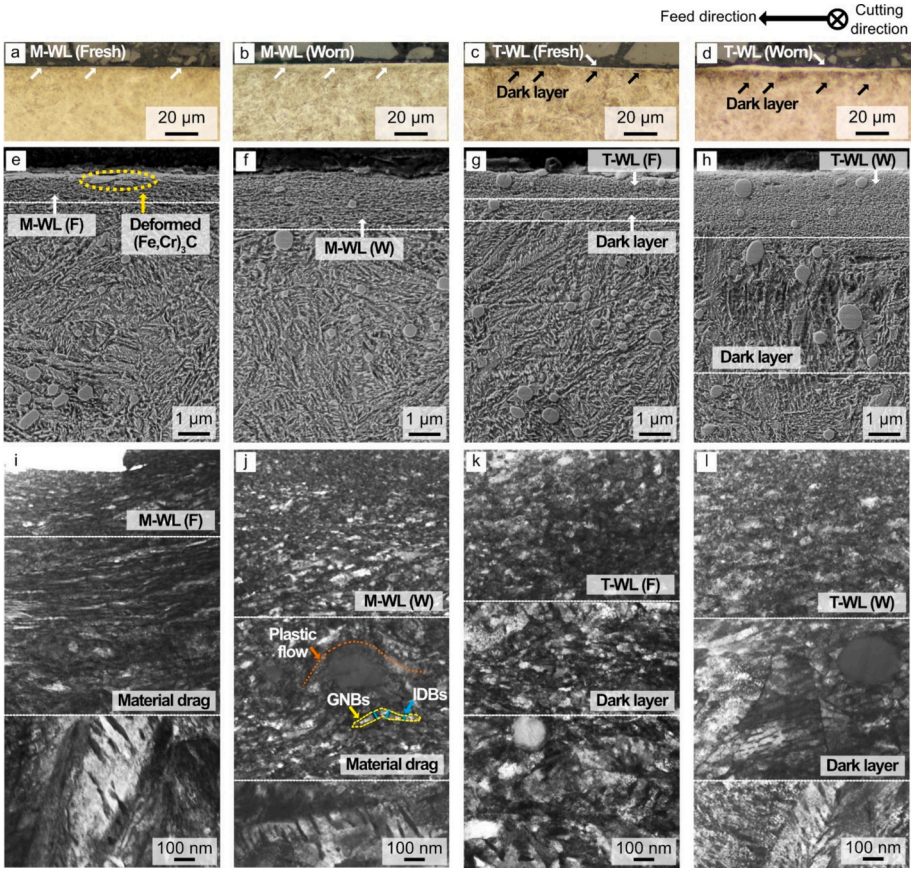

Fig. 5. (a-d) LOM (e-h) SE-SEM and (i-l) STEM-in-SEM BF images from the surface to the bulk. (e) M-WL (F) region containing deformed μm-sized (Fe, Cr)$_3$C cementite precipitates, highlighted with dotted yellow lines. (f) M-WL (W) region. (g) T-WL (F) region with dark layer underneath. (h) T-WL (W) and dark layer region with increased thickness. (i) Nanocrystalline grains observed in the M-WL (F) region, accompanied by thin lamellar grains in the material drag zone. (j) Nanocrystalline grains observed in the M-WL (W) region with the lamellar grains in the material drag region exhibiting geometrically necessary boundaries (GNBs) highlighted in yellow dotted line and incidental dislocation boundaries (IDBs) displayed in blue lines, indicative of a grain subdivision mechanism. Plastic flow of the lamellar grains were indicated by the orange dotted line above the (Fe, Cr)$_3$C cementite. (*k*,*l*) T-WL (F) and (W) regions exhibiting nanocrystalline grains.

material. In contrast, the absence of a dark layer beneath the M-WLs suggests a dominant mechanical effect with minimal thermal influence. Under both the cutting conditions, the thickness of the affected white layer region on the machined surface increased when using a worn insert (Fig. 5f,h) compared to using fresh inserts (Fig. 5e,g). Specifically, with fresh inserts, the M-WL/T-WL thickness was ~1 μm, whereas worn inserts led to thicknesses ranging from 1.5 to 3 μm. These findings confirm that hard turning induces microstructural changes within the surface layer, leading to the formation of white layers due to the thermo-mechanical interaction between the cutting tool and the workpiece. The extent of this interaction dictates whether a M-WL (dominated by mechanical effects, no dark layer) or a T-WL (dominated by thermal effects, with a dark layer) is formed. Both M-WLs and T-WLs exhibit a distinct morphology compared to the unaffected bulk microstructure, primarily due to the grain refinement. Fig. 5e,f illustrates that the M-WL microstructure is characterized by fragmented, elongated grains aligned in the feed direction, indicating significant plastic deformation. Additionally, the μm-sized (Fe, Cr)$_3$C cementite particles located closer to the

machined surface (as shown in Fig. 5e, marked by yellow dotted lines) show evidence of plastic deformation and fragmentation, resulting in an increased aspect ratio. In contrast, in the T-WLs (Fig. 5 g,h), plastic deformation of the μm-sized $(Fe, Cr)_3C$ particles is not clearly observed. However, based solely on LOM and SE-SEM observations, a definitive distinction between the M-WL and T-WL microstructures remains unclear, highlighting the need for further detailed analysis.

To investigate the microstructural features in more detail, STEM-in-SEM BF imaging is performed on electron-transparent lamellae prepared via FIB lift-out, as shown in Figs. 5i-l. These images clearly reveal a microstructural gradient from the machined surface into the bulk material across all cutting conditions. Focusing on M-WLs, with a fresh insert (Fig. 5i), elongated nanocrystalline grains are evident closest to the surface. Beneath this region, the material drag region featured elongated, thin lamellar-structured grains aligned with the feed direction, a feature not clearly resolved by SEM-SE imaging. Below the material drag region, the unaffected tempered martensitic structure is observed. When a worn insert is used (Fig. 5j), the M-WL (W) exhibited an increased thickness of nanocrystalline grains. Furthermore, the material drag region beneath it displayed lamellar grains with a thickness of 30–50 nm. This suggests that the intensity of plastic deformation decreases with depth and a transition from nanocrystalline to elongated lamellar grains occurs. As shown in Fig. 5j, these lamellar grains within the material drag region exhibit geometrically necessary boundaries (GNBs) highlighted in yellow dashed line and incidental dislocation boundaries (IDBs) displayed in blue lines, indicative of a grain subdivision mechanism. Additionally, these lamellar grains in the material drag region showed evidence of plastic flow around the μm-sized $(Fe, Cr)_3C$ cementite precipitate as illustrated with the orange dotted line in Fig. 5j. In contrast, T-WLs (Fig. 5 k,l) show a different microstructural gradient. While nanocrystalline grains are present at the machined surface, no lamellar grains are observed at increasing depths, suggesting the absence of severe plastic deformation. Moreover, within the dark layer of the T-WL (W) as seen in Fig. 5 l, neither the lath martensite nor the microstructure surrounding the μm-sized $(Fe, Cr)_3C$ cementite precipitates showed significant signs of plastic deformation, further differentiating the formation mechanisms of T-WLs from M-WLs.

3.3. TKD pattern matching on white layers

To enable a more quantitative assessment of white layers beyond the resolution limits of STEM-in-SEM BF imaging, TKD analysis is conducted with a step size of 10 nm from the machined surface to a depth of approximately 4 μm, as shown in Fig. 6a-d. The AztecCrystal MapSweeper pattern matching technique is applied to all four samples to enhance the accuracy from Hough-based indexing. For all the analyses, an inverse pole figure (IPF) map parallel to the cutting direction (*Vc*) was overlaid on the band contrast image, with a HAGB misorientation threshold of >10°. In the IPF maps, dark regions represent unindexed areas (zero solutions) with low-quality band contrast, where the pattern matching technique could not reliably resolve the stored Kikuchi patterns during image correlation. Across all four IPF orientation maps, it is evident that the machined surface exhibits significant grain refinement with a nanocrystalline grain structure compared to the bulk material, consistent with our STEM-in-SEM observations. For the M-WL (F) sample machined with *Vc*: 60 m/min and f: 0.05 mm/rev using a fresh insert, a distinct change in crystallographic grain orientation is observed near the machined surface as shown in Fig. 6a with black arrows, indicating a deviation from the ⟨101⟩ orientation of the block/packet grain. When machined with similar cutting parameters but using a worn insert (Fig. 6b), the TKD analysis confirms the material drag behaviour beneath the nanocrystalline M-WL, as highlighted within the black rectangular box. This region consists of a heavily deformed martensitic structure aligned parallel to the feed direction. Furthermore, the material drag region, which STEM-in-SEM BF imaging (Fig. 5j) revealed to comprise lamellar grains with GNBs and IDBs, is now visible through TKD pattern matching in the black box of Fig. 6b. In contrast, when machining with higher cutting parameters (*Vc*: 110 m/min, *f*: 0.2 mm/rev), the IPF orientation maps of the T-WLs show no presence of lamellar grains, corresponding to the STEM-in-SEM BF imaging observations. This strongly suggests a higher thermal effect dominating over mechanical effects closer to the machined surface in these conditions. Moreover, both STEM-in-SEM and TKD analyses reveal no evidence of grain refinement or grain subdivision within the dark layer region.

To further study the microstructural features, higher magnification TKD analysis with a step size of 5 nm, combined with advanced pattern matching was performed on the nanocrystalline white layer regions for both the M-WL (W) and T-WL (W) cutting conditions, as presented in Fig. 7a,b, respectively. As previously observed in Fig. 6b,d compared to Fig. 6a,c, the use of worn inserts significantly increased the thickness of the affected region, providing a robust basis for further investigation into grain size and morphology in these specific white layers. Grain boundaries with misorientation angles between 2° and 10° are classified as low-angle grain boundaries (LAGBs), while those exceeding 10° are

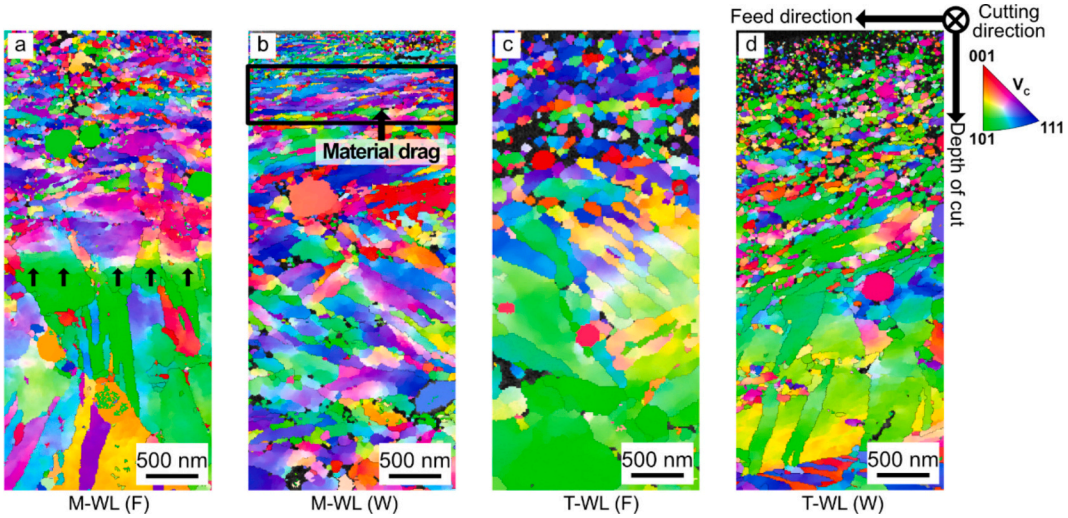

Fig. 6. The IPF orientation maps parallel to the cutting direction from the machined surface to a depth of ~4 μm. (a) M-WL (F) region. (b) Material drag in the M-WL (W) region, highlighted by a black rectangular box.
(c) T-WL (F) region, and (d) T-WL (W) region.

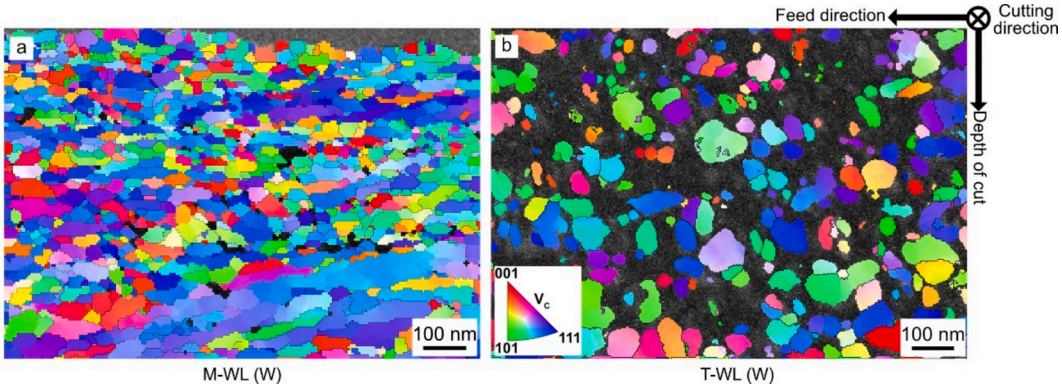

Fig. 7. IPF orientation maps of nanocrystalline white layers. (a) M-WL (W) and (b) T-WL (W).

considered HAGBs indicated by black lines. In the M-WL (W) sample shown in Fig. 7a, the nanocrystalline grains exhibited a distinct rectangular morphology with an average aspect ratio of 2.9 ± 1.1 and an area-weighted mean equivalent circle diameter of 58 ± 18 nm. The combination of a higher aspect ratio and nanocrystalline grains strongly indicates the occurrence of grain elongation and fragmentation resulting from the intense plastic strain experienced at the machined surface. In contrast, the nanocrystalline grains within the T-WL (W) sample have an aspect ratio of 1.7 ± 0.5 and an area-weighted mean grain size of 58 ± 20 nm. While the average grain size is similar to that observed in M-WL (W), the distinct difference in grain morphology suggests that these white layers form through fundamentally different mechanisms.

4. Discussions

In hard turning, material removal is primarily driven by the shearing action of a single-point, geometrically well-defined PCBN cutting tool. The intense thermo-mechanical interactions occurring at the tertiary cutting zone strongly influenced by parameters such as cutting speed, feed rate, and tool geometry (including chamfer angle, edge radius, nose radius, and flank wear) play a critical role in altering the surface integrity of the machined workpiece. These interactions, combined with the material's thermal properties (e.g., thermal conductivity and specific heat capacity), result in localized variations in strain, strain rate, shear angle, and temperature, all of which contribute to microstructural evolution at the surface [29–32]. The results clearly reveal that variations in cutting parameters lead to distinct formation mechanisms for M-WL and T-WL in AISI 52100 tempered martensitic steel. This section focuses on the M-WL evolution, plastically deformed μm-sized $(Fe, Cr)_3C$ cementite precipitates and compares their development with that of T-WL. This study describes an attempt to characterize the highly deformed nanocrystalline grains generated by hard turning in high-carbon tempered martensitic steel (AISI 52100), using advanced TKD pattern matching technique for the first time.

The M-WL was observed after hard turning at a low cutting speed (*Vc*) of 60 m/min and a low feed rate (*f*) of 0.05 mm/rev (Fig. 5e,i). Additionally, a tool flank wear of ~0.2 mm contributed to an increased thickness of this altered region (Fig. 5f,j). As shown in Fig. 7a, the M-WL exhibits fragmented, rectangular nanocrystalline grains. Beneath this layer, a distinct material drag region is present, characterized by elongated lamellar grains surrounded by geometrically necessary boundaries (GNBs) and divided by incidental dislocation boundaries (IDBs), as seen in Fig. 5i,j and highlighted in Fig. 6b (black box). These types of lamellar grains are typically found in severe plastic deformation processes like surface mechanical rolling treatment [33], cold rolling [34], accumulative roll bonding [35], and in high strain rate adiabatic shear bands [9,10]. As reported in previous work [11], this gradient microstructure comprising nanocrystalline grains at the machined surface that are transitioning to elongated lamellar grains in the subsurface resulted in a substantial hardness increase of ~26% and ~ 7% compared to the bulk material. These observations indicate the significant role of shear-induced mechanisms in promoting the fragmentation of elongated lamellar grains and subsequent structural refinement near the machined surface, driven by increased plastic deformation. During hard turning of AISI 52100 steel, the process induces extreme conditions, with shear strains ranging from 1 to 10, strain rates between 10^4 and 10^6 s^{-1} and cutting zone temperatures reaching up to 1200 °C [36–38]. Additionally, surface cooling rates can be as high as 10^4–10^5 °C/s [39]. According to Hosseini et al. [39], hard turning of AISI 52100 steel at a *Vc* of 30 m/min and *f* of 0.08 mm/rev generated cutting temperatures of ~510 °C with a fresh insert and ~ 540 °C with a worn insert (VB ~0.2 mm). While cutting temperatures were not directly measured in this study, similar or slightly higher values are expected for the tested condition (*Vc* = 60 m/min, *f* = 0.05 mm/rev). These temperatures remain below the austenitization threshold (~750 °C) and the dynamic recrystallization temperature (~712 °C, or ~ 0.5 Tm) [10]. At temperatures below the dynamic recrystallization threshold, severe plastic deformation promotes dynamic recovery, which serves as the primary mechanism for the formation of nanocrystalline grains in M-WLs. This phenomenon has been supported by few studies [5–7,12]. From the metal cutting perspective, at a low feed rate of 0.05 mm/rev, the uncut chip thickness becomes much smaller than the tool tip radius, resulting in a highly negative effective rake angle. This tool geometry subjects the material ahead of the cutting edge to generate intense compressive stresses [40]. Furthermore, the low *Vc* of 60 m/min leads to higher cutting forces as there is less of a thermal softening effect in shearing the material. As a result, a larger volume of material undergoes extensive plastic deformation before forming a thin chip [40]. In this study, the use of a 35° chamfered angle results in a more negative effective rake angle, which alters the shear angle and contributes to a larger stagnation zone ahead of the cutting edge. This potentially increases the volume of deformed material that flows into the machined surface [41]. Furthermore, as reported in our previous work on residual stress measurements under similar cutting parameters [11], the M-WL (F) condition exhibited a surface compressive residual stress of −771 MPa, whereas the M-WL (W) condition exhibited a significantly higher compressive residual stress of −1351 MPa along the feed direction. As discussed above, these observed surface compressive residual stresses are primarily attributed to the predominance of severe plastic deformation. Similar findings were reported by Dahlman et al. [2], who demonstrated that a more negative rake angle increases the extent of plastic deformation in the workpiece. These combined effects of tool geometry and cutting parameters led to the formation of the M-WL.

From the microstructural perspective, the prior austenite grain is transformed into a hierarchical martensitic microstructure comprising packets, blocks, and laths [34,42]. EBSD analysis of the initial state (Fig. 4b) reveals a fine-grained structure with a block size of 1.9 ± 0.6 μm, represented by HAGBs with >10° misorientation. Furthermore, as

shown in the bulk region of Fig. 5i, the tempered martensite lath width is ~300–400 nm and contain rod-like tempered cementite within them. During hard turning, these laths undergo extensive subdivision into subgrains and realignment along the shear direction due to intense plastic deformation as shown in Fig. 8a with black dashed lines. As the material approaches the machined surface, within what we termed the material drag region, the combined effects of increasing strain, strain rate, and temperature lead to the formation of elongated structures. These are the lamellar grains, enriched with both geometrically necessary boundaries (GNBs) and incidental dislocation boundaries (IDBs), clearly visible in the STEM-in-SEM BF image in Fig. 9a. Hansen and Mehl [43], along with Hughes et al. [44,45] extensively studied the microstructure evolution in the deformed metals and named the formation process as the grain subdivision mechanism. GNBs develop between regions exhibiting different strain patterns to accommodate variations in lattice rotation. Such differences in strain patterns may arise from changes in the active slip systems, variations in the partitioning of slip activity within the same slip systems, or differences in the local strain level. These local variations promote, on average, compatible deformation involving fewer slip systems and reduced dislocation interactions, thereby lowering the stored energy. IDBs, on the other hand, form through the trapping of gliding dislocations. Multiple IDBs are typically developed within each lamellar grain divided by GNBs and tend to adopt low energy configurations [43–45]. Huang et al. [46] previously demonstrated that cold rolling can transform lath martensite into cell-block structures characterized by GNBs and IDBs. A similar process is observed in the material drag region, where the lath martensite undergoes subdivision into several GNBs and IDBs by progressively replacing the original lath boundaries. This reflects the progressive accommodation of strain under severe plastic deformation and is believed to represent the initial stage in M-WL formation. The observed average lamellar grain size of ~30–50 nm in the M-WL reflects the concept of grain saturation, typical of severe plastic deformation. Thermodynamically, further refinement beyond this size is hindered by the increasing grain boundary energy that counteracts the energy reduction associated with dislocation annihilation and establish a stable grain size limit under our processing conditions [47]. However, we note the presence of isolated, extremely fine grains of ~10 nm in localized regions (Fig. 9c), for which we currently do not have a definitive explanation. Similar observations were also reported by Huang et al. [46] of continued refinement without a clear saturation limit. The quantitative TKD pattern matching analysis offered new insights into the grain refinement mechanisms within M-WL. As depicted in Fig. 8b, misorientation analysis was performed on a representative lamellar grain. As shown in Fig. 8c, the point-to-point misorientation (black line) across this lamellar grain revealed subgrain structures with IDBs, characterized by LAGBs. While the point-to-origin misorientation (red line) showed a cumulative misorientation reaching approximately 13°. The dark lines surrounding the lamellar grain in Fig. 8b represent the GNBs, characterized by HAGBs. Typically, GNBs exhibit either low or high misorientation angles. However, under increasing strain and strain rate, GNBs typically evolve from low to predominantly high angle misorientation, while IDBs continue to exhibit low misorientation angle. As reported by Hansen and Mehl [43], the misorientation angle of both GNBs and IDBs follows a power-law relationship with strain. At medium to high strain levels, GNBs commonly develop into HAGBs (>10°), whereas IDBs exhibit LAGBs which is consistent with the observations in our study.

As strain and strain gradients intensify near the machined surface, grain subdivision progresses, increasing LAGB misorientations within IDBs and ultimately leading to the formation of distinct, rectangular nanocrystalline grains (Fig. 9b). This fragmentation is primarily driven by dynamic recovery, which facilitates the transformation of LAGBs into new HAGBs, resulting in nanocrystalline grains with HAGBs, as seen in

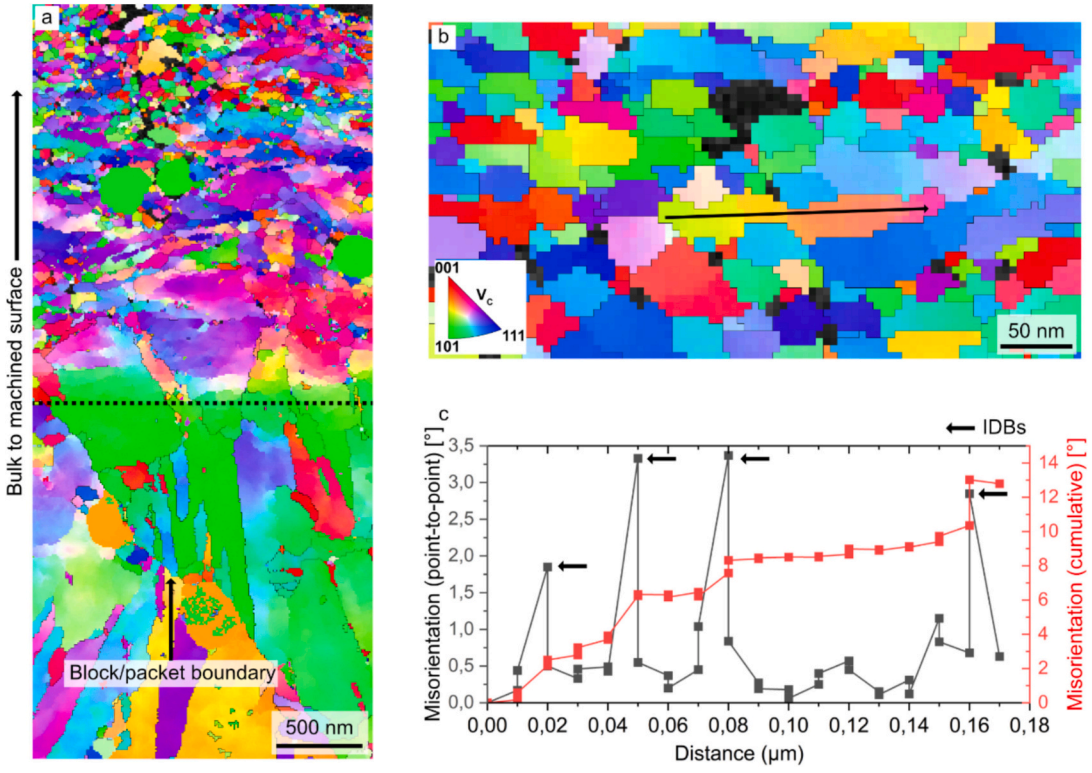

Fig. 8. Revealing grain subdivision mechanism using TKD pattern matching. (a) The influence of hard turning on the orientation of block/packet structure, highlighted by black dashed lines. (b) Rectangular lamellar grain observed within the material drag region, exhibiting varying IPF orientations. (c) The misorientation point-to-point and cumulative line profile analysis corresponding to the black arrow in (b) with the point-to-point analysis indicating the low angle IDBs in the lamellar grain.

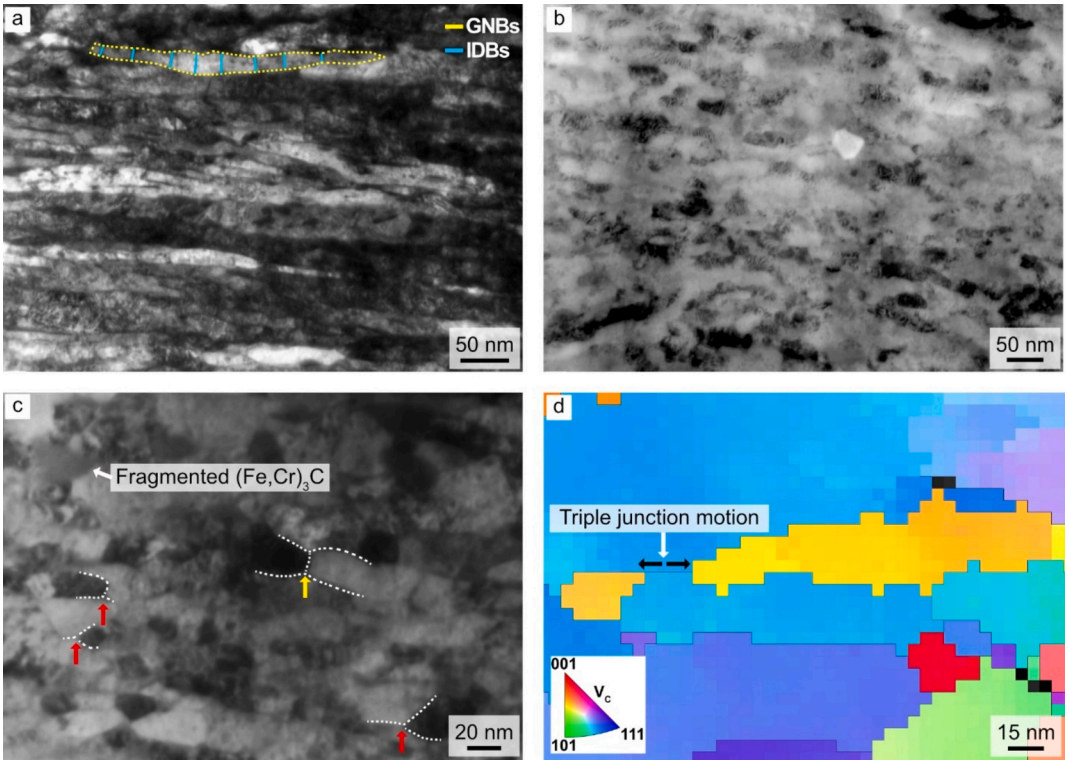

Fig. 9. Dynamic recovery assisted triple junction motion. (a) Lamellar grains in the material drag region of the M-WL, with geometrically necessary boundaries (GNBs) shown in yellow and incidental dislocation boundaries (IDBs) in blue. (b) As strain increases closer to the machined surface, the lamellar grains evolve into rectangular nanocrystalline grains in the M-WL region. (c) High-magnification image of the nanocrystalline grains in the M-WL region reveal H-type (yellow arrow) and Y-type (red arrow) junctions. (d) TKD pattern matching reveals dynamic recovery assisted triple junction motion, indicated by black arrows. (For interpretation of the references to colour in this figure legend, the reader is referred to the web version of this article.)

Fig. 7a. The formation of nanocrystalline grains in the M-WL is further supported by the mechanically assisted triple junction motion, a known dynamic recovery mechanism reported in severely deformed cold rolled aluminium [14,15,48,49]. Yu et al. [15] categorized triple junctions based on their morphology: Y junctions, which connect three lamellar boundaries (GNBs); and H and r junctions, which involve IDBs. In the present work, BF STEM-in-SEM imaging (Fig. 9c) reveals Y-junctions (indicated by red arrows) and an H-junction (yellow arrow) in the M-WL region. Multiple triple junctions are visible in this image, highlighting their active role in the microstructural evolution of the M-WL region. The lamellar grains formed through grain subdivision in the material drag region undergo localized shear deformation and subsequently break up due to triple junction migration [48]. This migration process replaces two lamellar boundaries with one and eliminates associated IDBs and dislocations in the displaced region, while preserving the rectangular morphology of the nanocrystalline structure [15]. Consequently, this behaviour reduces the stored strain energy in the deformed material, characteristic of a dynamic recovery mechanism [14]. However, there is no current theory that can fully explain the extremely rapid boundary migration during hard turning, which occurs within a few hundred microseconds. TKD pattern matching (Fig. 9d) in combination with STEM-in-SEM BF (Fig. 9c) further confirms that lamellar grain fragmentation occurs through mechanically assisted triple junction motion, with black arrows indicating the direction of this triple junction motion. Triple junction motion is often linked to structural coarsening during dynamic recovery under conventional conditions [47]. However, pinning of triple junctions by solute atoms, dislocations, or other defects plays a crucial role by immobilizing these junctions, thereby stabilizing the grain boundary network and suppressing grain coarsening [50,51]. This pinning allows the fragmented nanocrystalline grains to persist without coalescing unless a high driving force (e.g., high temperature, time, or loss of pinning) is present, explaining their smaller or similar size compared to the original lamellar structure observed in M-WL. Such mechanisms highlight the interplay between triple junction dynamics and strong pinning, which promotes structural stability of the refined grains rather than coarsening in severe deformation regimes under adiabatic conditions as observed in the current study.

As shown in Fig. 5j, the lamellar grains in the material drag region exhibit plastic flow around (Fe, Cr)$_3$C cementite particles due to severe plastic deformation. A similar behaviour was reported by Qin et al. [52] during high-pressure torsion at an equivalent strain of 9.3. In the M-WL region, increasing strain and strain rate likely cause local stress concentrations at the matrix/cementite interface to exceed the shear strength of the μm-sized (Fe, Cr)$_3$C precipitates, leading to their deformation and fragmentation (Figs. 5a and 9c). A similar observation was reported by Zhang et al. [33] in their study of surface mechanical rolling treatment (SMRT) on AISI 52100 martensitic steel. By analysing the behaviour of the material drag zone, the M-WL microstructure, and the deformation around μm-sized (Fe, Cr)$_3$C cementite precipitates, our results indicate that the microstructure evolution in M-WLs during hard turning at low cutting speed and feed rate is primarily initiated by the grain subdivision process, followed by mechanically assisted triple junction motion dynamic recovery mechanism resulting in the rectangular nanocrystalline grains. This study presents the first direct TKD-based evidence for confirming the proposed formation mechanism of nanocrystalline M-WLs in tempered martensitic steel.

In contrast to the M-WL, the T-WL exhibit a distinct microstructural evolution, primarily due to the higher cutting speed and feed rate. The observed T-WLs feature nanocrystalline grains at the machined surface, and by a characteristic dark layer beneath it, as evident in Figs. 5c,d,f, and g. A critical observation is that lamellar grains are absent within the T-WL, suggesting that the grain subdivision mechanism, which is prominent in M-WL formation, is not active here. Instead, the dark layer, as revealed by the STEM-in-SEM BF image (Fig. 5 l), contains largely

unaffected μm-sized (Fe, Cr)$_3$C cementite precipitates and retains its original lath structure. Furthermore, a comparison of the high magnification TKD pattern matching IPF orientation maps shows that the nanocrystalline grains in the T-WL (Fig. 7b) possess a lower aspect ratio compared to the more fragmented, rectangular grains in M-WL (Fig. 7a). These distinctions point towards a dominant thermal influence rather than severe plastic deformation in the formation of T-WL. At the higher feed rate of 0.2 mm/rev, the observed increase in cutting temperature is directly attributable to the corresponding rise in chip thickness and cutting forces. The intensified material removal rate generates substantial heat within the cutting zone, leading to elevated thermal loads over a short processing time [1]. Due to this and as reported in our previous work [11], the T-WL (F) and T-WL (W) conditions exhibited lower surface compressive residual stresses compared to the M-WLs. Notably, the T-WL (W) condition showed a tensile residual stress of 530 MPa along the cutting direction. Hosseini et al. [39], reported that at 110 m/min and 0.08 mm/rev, temperatures during T-WL formation in AISI 52100 steel reached ~820 °C (fresh insert) and ~900 °C (worn insert), exceeding both the austenitization (~750 °C) and dynamic recrystallization (~712 °C) thresholds (~0.5 times the melting temperature). Machining at cutting parameters of *Vc*: 110 m/min and *f*: 0.2 mm/rev occurs within just a few microseconds, during which the surface temperature exceeds the phase transformation threshold. Under these conditions, the formation of nanocrystalline grains results from the continuous dynamic recrystallization (CDRX) mechanism. This process involves the continuous increase of boundary misorientation through the rotation of subgrains within the re-austenitized phase, followed by rapid quenching resulting in nanocrystalline untempered martensite [9,11,39]. Furthermore, the predominant temperature gradient effect resulted in the formation of over-tempered martensite, observed as the dark layer in Fig. 5d, which exhibited a hardness that is ~16% lower than the bulk material [11]. Fig. 10 schematically illustration the above mentioned M-WL microstructure evolution process in comparison to the T-WL.

Furthermore, as reported by Barry and Byrne [5], the re-austenitization process involved in the formation of the T-WL leads to an increased austenite content. However, in the present study, retained austenite was not detected in the T-WL region. Simon [53] reported a similar observation, finding no clear evidence of retained austenite using EBSD in his study of white etching layers formed during deep hole drilling. Despite the application of pattern matching, several TKD patterns particularly in T-WL regions could not be reliably indexed. This issue is primarily attributed to the increased thickness of the FIB lamella due to curtaining effect, and highly strained deformed regions that subsequently result in the reduction of TKD pattern quality. To ensure the reliability of the results, a suitable minimum threshold for image correlation (between experimental and simulated patterns) is crucial to prevent incorrect solutions from being obtained for the poorest patterns in the dataset. A higher normalized cross-correlation R threshold (e.g., $R = 0.25$) would on the one hand, reduce the success rate for indexing, but on the other hand, it would eliminate unreliable solutions. In contrast, a lower R threshold (e.g., $R = 0.1$) would increase the indexing success rate at the expense of data reliability. The chosen value of R = 0.25 provided an optimal balance between these two options. Further, Table 2 summarizes the relationship between the cutting parameters, the resulting WL type, and the measured WL thickness to clearly illustrate the process-structure correlation.

Table 2
Summary table providing the process-structure relationship.

Cutting speed (V_c)	Feed rate (f)	WL type	WL thickness (fresh/worn)	DL thickness (fresh/worn)	Temperatures [39]
60 m/min	0,05 mm/rev	M-WL	~1 μm / 3 μm	NA	~510 °C / 540 °C
110 m/min	0,2 mm/rev	T-WL	~1 μm / 3 μm	~1 μm / 4 μm	~820 °C / 900 °C

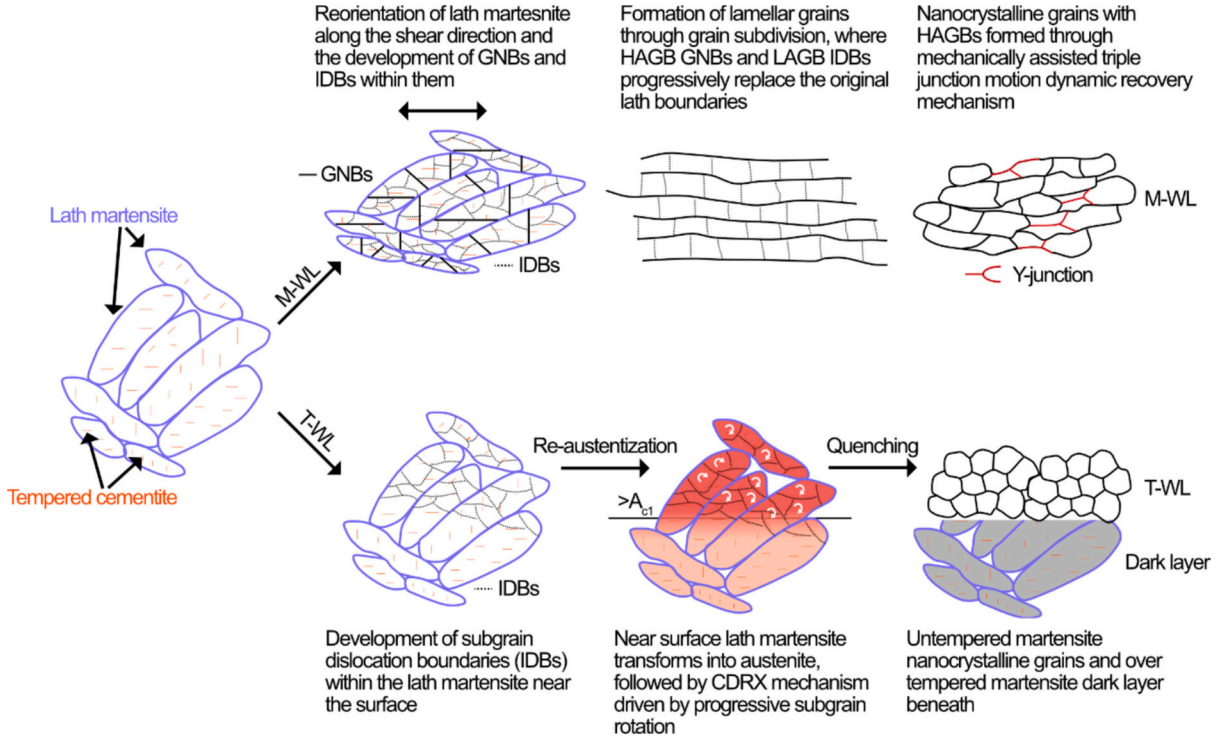

Fig. 10. Schematic illustration of the M-WL microstructure evolution initiated by the grain subdivision process, followed by mechanically assisted triple junction motion dynamic recovery mechanism and T-WL driven by continuous dynamic recrystallization mechanism in association with reverse martensite transformation.

5. Conclusions

To understand the complex microstructural evolution of the nanocrystalline grains under hard turning conditions, we utilized advanced techniques like SEM, STEM-in-SEM and TKD pattern matching analysis. This study primarily aimed to investigate the microstructural evolution of M-WLs in AISI 52100 tempered martensitic steel, from the machined surface into the unaffected bulk, to understand its gradient nature. The findings were systematically compared with the well-established T-WL formed via dynamic recrystallization. The following conclusions are drawn from this study:

- The M-WL features nanocrystalline grains at the surface, transitioning to elongated lamellar grains in the underlying material drag region. In contrast, the T-WL is characterized by nanocrystalline grains followed by a dark, over-tempered layer. While both M-WL and T-WL exhibit a similar mean average grain size of ~58 nm, their differing aspect ratios (2.9 ± 1.1 for M-WL, 1.7 ± 0.5 for T-WL) strongly suggest distinct formation mechanisms.
- Quantitative data obtained through TKD pattern matching analysis, confirms the presence of lamellar grains beneath the M-WL, marked by the formation of high-angle geometrically necessary boundaries (GNBs) and low-angle incidental dislocation boundaries (IDBs). As strain increases closer to the hard-turned surface, these lamellar grains evolve into rectangular nanocrystalline grains, within which we observed both H and Y triple junctions.
- Furthermore, we found clear evidence of intensive plastic strain in the μm-sized $(Fe, Cr)_3C$ cementite precipitates within the M-WL. The lamellar grains in the material drag region exhibited plastic flow behaviour around these particles, a behaviour absent in T-WLs.
- Based on these new observations, we propose that the microstructure evolution in M-WL during hard turning is primarily initiated by grain subdivision process leading to lamellar grain formation. This is then subsequently followed by mechanically assisted triple junction motion, a dynamic recovery mechanism that ultimately leads to the formation of the HAGB rectangular nanocrystalline grains.

This study additionally highlights the novel attempt in characterizing the highly strained nanocrystalline grains on hard turned surfaces of AISI 52100 tempered martensitic steel. We emphasize the critical role of advanced TKD pattern matching, which significantly improved the indexing accuracy compared to the conventional Hough transform and provided the first direct TKD-based validation of the detailed M-WL microstructural evolution mechanism.

CRediT authorship contribution statement

Sahith Kokkirala: Writing – original draft, Visualization, Validation, Methodology, Investigation, Formal analysis, Conceptualization. **Seyed B. Hosseini:** Writing – review & editing, Supervision, Funding acquisition, Conceptualization. **Uta Klement:** Writing – review & editing, Supervision, Resources, Project administration, Funding acquisition, Conceptualization.

Declaration of competing interest

The authors declare that they have no known competing financial interests or personal relationships that could have appeared to influence the work reported in this paper.

Acknowledgements

This work is part of the Turn2Flex project (Vinnova 2021-01274), under the Production 2030 strategic innovation program, funded by VINNOVA, the Swedish Energy Agency, Formas and of the Hybrid 60 project (Ultrahigh-strength surfaces on novel corrosion resistant hybrid steel) funded by the Swedish Research Council (2023-04410). Special thanks to Hirotsugu Iwasaki and Wolfgang Neuhs (Sumitomo Electric Hartmetall GmbH) for their support with hard turning experiments. We gratefully acknowledge Dr. Thorsten Meiners (Oxford Instruments NanoAnalysis) for introducing us to the pattern matching technique and providing valuable training. This work was performed in part at the Chalmers Material Analysis Laboratory, CMAL.

Data availability

Data will be made available on request.

References

[1] J. Hua, R. Shivpuri, X. Cheng, V. Bedekar, Y. Matsumoto, F. Hashimoto, T. R. Watkins, Effect of feed rate, workpiece hardness and cutting edge on subsurface residual stress in the hard turning of bearing steel using chamfer + hone cutting edge geometry, Mater. Sci. Eng. A 394 (2005) 238–248, https://doi.org/10.1016/j.msea.2004.11.011.
[2] P. Dahlman, F. Gunnber, M. Jacobson, The influence of rake angle, cutting feed and cutting depth on residual stresses in hard turning, J. Mater. Process. Technol. 147 (2004) 181–184, https://doi.org/10.1016/j.matprotec.2003.12.014.
[3] S. Kokkirala, J. Holmberg, U. Klement, R. Lundstrom, H. Iwasaki, S.B. Hosseini, Effect of cutting parameters on the generated surface integrity of hard-turned martensitic AISI 52100 bearing steel, Procedia CIRP 115 (2022) 154–159, https://doi.org/10.1016/j.procir.2022.10.066.
[4] A. Ramesh, S.N. Melkote, L.F. Allard, L. Riester, T.R. Watkins, Analysis of white layers formed in hard turning of AISI 52100 steel, Mater. Sci. Eng. A 390 (2005) 88–97.
[5] J. Barry, G. Byrne, TEM study on the surface white layer in two turned hardened steels, Mater. Sci. Eng. A 325 (2002) 356–364.
[6] S. Akcan, W.I.S. Shah, S.P. Moylan, P.N. Chhabra, S. Chandrasekar, H.T.Y. Yang, Formation of white layers in steels by machining and their characteristics, Metall. Mater. Trans. A Phys. Metall. Mater. Sci. 33 (2002) 1245–1254.
[7] S.B. Hosseini, U. Klement, Y. Yao, K. Ryttberg, Formation mechanisms of white layers induced by hard turning of AISI 52100 steel, Acta Mater. 89 (2015) 258–267, https://doi.org/10.1016/j.actamat.2015.01.075.
[8] S.B. Hosseini, U. Klement, A descriptive phenomenological model for white layer formation in hard turning of AISI 52100 bearing steel, CIRP J. Manuf. Sci. Technol. 32 (2021) 299–310, https://doi.org/10.1016/j.cirpj.2021.01.014.
[9] C.Z. Duan, L.C. Zhang, Adiabatic shear banding in AISI 1045 steel during high speed machining: mechanisms of microstructural evolution, Mater. Sci. Eng. A 532 (2012) 111–119, https://doi.org/10.1016/j.msea.2011.10.071.
[10] S.X. Li, P.C. Zhao, Y.N. He, S.R. Yu, Microstructural evolution associated with shear location of AISI 52100 under high strain rate loading, Mater. Sci. Eng. A 662 (2016) 46–53, https://doi.org/10.1016/j.msea.2016.03.050.
[11] S. Kokkirala, U. Klement, J. Holmberg, H. Iwasaki, J. Manuel, B. Bermejo, S. Kimming, S.B. Hosseini, Understanding the development of mechanically and thermally induced white layers in AISI 52100 steel during hard turning : process-microstructure-property relationship, J. Mater. Res. Technol. 38 (2025) 1185–1197, https://doi.org/10.1016/j.jmrt.2025.07.293.
[12] B. Zhang, W. Shen, Y. Liu, X. Tang, Y. Wang, Microstructures of surface white layer and internal white adiabatic shear band, Wear 211 (1997) 164–168, https://doi.org/10.1016/S0043-1648(97)00099-9.
[13] R. Pippan, S. Scheriau, A. Taylor, M. Hafok, A. Hohenwarter, A. Bachmaier, Saturation of fragmentation during severe plastic deformation, Annu. Rev. Mat. Res. 40 (2010) 319–343, https://doi.org/10.1146/annurev-matsci-070909-104445.
[14] T. Yu, N. Hansen, X. Huang, A. Godfrey, Observation of a new mechanism balancing hardening and softening in metals, Mater. Res. Lett. 2 (2014) 160–165, https://doi.org/10.1080/21663831.2014.886308.
[15] T. Yu, N. Hansen, X. Huang, Recovery by triple junction motion in aluminium deformed to ultrahigh strains, Proc. R. Soc. A Mat. Phys. Eng. Sci. 467 (2011) 3039–3065, https://doi.org/10.1098/rspa.2011.0097.
[16] O. Renk, P. Ghosh, R. Pippan, Generation of extreme grain aspect ratios in severely deformed tantalum at elevated temperatures, Scr. Mater. 137 (2017) 60–63, https://doi.org/10.1016/j.scriptamat.2017.04.024.
[17] O. Renk, A. Hohenwarter, S. Wurster, R. Pippan, Direct evidence for grain boundary motion as the dominant restoration mechanism in the steady-state regime of extremely cold-rolled copper, Acta Mater. 77 (2014) 401–410, https://doi.org/10.1016/j.actamat.2014.06.010.
[18] A.J. Schwartz, M. Kumar, B.L. Adams, D.P. Field, Electron backscatter diffraction in materials science, Springer, 2009. https://scholar.google.com/scholar_lookup?title=ElectronBackscatterDiffractioninMaterialsScience&author=A.J.Schwartz&publication_year=2010.
[19] P.W. Trimby, Orientation mapping of nanostructured materials using transmission Kikuchi diffraction in the scanning electron microscope, Ultramicroscopy 120 (2012) 16–24, https://doi.org/10.1016/j.ultramic.2012.06.004.
[20] A. Avishai, K. Abbasi, D. Wang, N. Avishai, D. Wu, V. Bedekar, S. Hyde, S. Sitzman, A. Heuer, Tackling characterization challenges in high deformation/stress steel alloys using transmission Kikuchi diffraction (TKD), Microsc. Microanal. 21 (2015) 2377–2378, https://doi.org/10.1017/s1431927615012660.

[21] V. Bedekar, R. Shivpuri, A. Avishai, R.S. Hyde, Transmission Kikuchi diffraction study of texture and orientation development in nanostructured hard turning layers, CIRP Ann. Manuf. Technol. 64 (2015) 73–76, https://doi.org/10.1016/j.cirp.2015.04.073.
[22] K. Nikolic, V.M. Ferreira, L. Malet, T. Depover, K. Verbeken, R.H. Petrov, Uncovering the white etching area and crack formation mechanism in bearing steel, Mater Charact 197 (2023) 112659, https://doi.org/10.1016/j.matchar.2023.112659.
[23] P.W. Trimby, Y. Cao, Z. Chen, S. Han, K.J. Hemker, J. Lian, X. Liao, P. Rottmann, S. Samudrala, J. Sun, J.T. Wang, J. Wheeler, J.M. Cairney, Characterizing deformed ultrafine-grained and nanocrystalline materials using transmission Kikuchi diffraction in a scanning electron microscope, Acta Mater. 62 (2014) 69–80, https://doi.org/10.1016/j.actamat.2013.09.026.
[24] G. Nolze, M. Jürgens, J. Olbricht, A. Winkelmann, Improving the precision of orientation measurements from technical materials via EBSD pattern matching, Acta Mater. 159 (2018) 408–415, https://doi.org/10.1016/j.actamat.2018.08.028.
[25] A. Winkelmann, B.M. Jablon, V.S. Tong, C. Trager-Cowan, K.P. Mingard, Improving EBSD precision by orientation refinement with full pattern matching, J. Microsc. 277 (2020) 79–92, https://doi.org/10.1111/jmi.12870.
[26] G. Cios, A. Winkelmann, T. Tokarski, P. Bala, Pattern matching workflows for EBSD data analysis: quartz chirality mapping, Mater Charact 224 (2025) 115076, https://doi.org/10.1016/j.matchar.2025.115076.
[27] P. Trimby, M. Al-Mosawi, M. Al-Jawad, S. Micklethwaite, Z. Aslam, A. Winkelmann, S. Piazolo, The characterisation of dental enamel using transmission Kikuchi diffraction in the scanning electron microscope combined with dynamic template matching, Ultramicroscopy 260 (2024) 113940, https://doi.org/10.1016/j.ultramic.2024.113940.
[28] S. Kokkirala, in: Chalmers University of Technology (Ed.), The Formation of White Layers and its Impact on Surface Integrity of Hard-Turned Tempered Martensitic Bearing Steels, 2024. https://research.chalmers.se/en/publication/541260.
[29] W. Zhang, K. Zhuang, Effect of cutting edge microgeometry on surface roughness and white layer in turning AISI 52100 steel, Procedia CIRP 87 (2020) 53–58, https://doi.org/10.1016/j.procir.2020.02.079.
[30] S. Liu, X. Wang, Z. Liu, Y. Wang, H. Chen, P. Wang, Microstructure and micromechanical properties evolution pattern of metamorphic layer subjected to turning process of carbon steel, Appl. Surf. Sci. 608 (2023) 154679, https://doi.org/10.1016/j.apsusc.2022.154679.
[31] Y.K. Chou, H. Song, Tool nose radius effects on finish hard turning, J. Mater. Process. Technol. 148 (2004) 259–268, https://doi.org/10.1016/j.jmatprotec.2003.10.029.
[32] B. Li, H. Liu, J. Zhang, B. Xu, W. Zhao, Multi-mechanism-based twinning evolution in machined surface induced by thermal-mechanical loads with increasing cutting speeds, Int. J. Mach. Tools Manuf. 192 (2023) 104074, https://doi.org/10.1016/j.ijmachtools.2023.104074.
[33] K. Zhang, Z.B. Wang, Strain-induced formation of a gradient nanostructured surface layer on an ultrahigh strength bearing steel, J. Mater. Sci. Technol. 34 (2018) 1676–1684, https://doi.org/10.1016/j.jmst.2017.12.012.
[34] R. Ueji, N. Tsuji, Y. Minamino, Y. Koizumi, Ultragrain refinement of plain low carbon steel by cold-rolling and annealing of martensite, Acta Mater. 50 (2002) 4177–4189, https://doi.org/10.1016/S1359-6454(02)00260-4.
[35] N. Tsuji, R. Gholizadeh, R. Ueji, N. Kamikawa, L. Zhao, Y. Tian, Y. Bai, A. Shibata, Formation mechanism of ultrafine grained microstructures: various possibilities for fabricating bulk nanostructured metals and alloys, Mater. Trans. 60 (2019) 1518–1532.
[36] A. Ramesh, S.N. Melkote, Modeling of white layer formation under thermally dominant conditions in orthogonal machining of hardened AISI 52100 steel, Int. J. Mach. Tools Manuf. 48 (2008) 402–414, https://doi.org/10.1016/j.ijmachtools.2007.09.007.
[37] D. Umbrello, J. Hua, R. Shivpuri, Hardness-based flow stress and fracture models for numerical simulation of hard machining AISI 52100 bearing steel, Mater. Sci. Eng. A 374 (2004) 90–100, https://doi.org/10.1016/j.msea.2004.01.012.
[38] S.P.F.C. Jaspers, J.H. Dautzenberg, Material behaviour in metal cutting: strains, strain rates and temperatures in chip formation, J. Mater. Process. Technol. 121 (2002) 123–135, https://doi.org/10.1016/S0924-0136(01)01227-4.
[39] S.B. Hosseini, T. Beno, U. Klement, J. Kaminski, K. Ryttberg, Cutting temperatures during hard turning—measurements and effects on white layer formation in AISI 52100, J. Mater. Process. Technol. 214 (2014) 1293–1300. https://linkinghub.elsevier.com/retrieve/pii/S0924013614000399.
[40] M.A. Elbestawi, A.K. Srivastava, T.I. El-Wardany, A model for Chip formation during machining of hardened steel, CIRP Ann. Manuf. Technol. 45 (1996) 71–76, https://doi.org/10.1016/S0007-8506(07)63019-4.
[41] M. Agmell, A. Ahadi, O. Gutnichenko, J.E. Ståhl, The influence of tool micro-geometry on stress distribution in turning operations of AISI 4140 by FE analysis, Int. J. Adv. Manuf. Technol. 89 (2017) 3109–3122, https://doi.org/10.1007/s00170-016-9296-7.
[42] H. Kitahara, R. Ueji, N. Tsuji, Y. Minamino, Crystallographic features of lath martensite in low-carbon steel, Acta Mater. 54 (2006) 1279–1288, https://doi.org/10.1016/j.actamat.2005.11.001.
[43] N. Hansen, R.F. Mehl, New discoveries in deformed metals, Metall. Mater. Trans. A 32 (2001) 2917–2935, https://doi.org/10.1007/s11661-001-0167-x.
[44] D.A. Hughes, N. Hansen, High angle boundaries formed by grain subdivision mechanisms, Acta Mater. 45 (1997) 3871–3886, https://doi.org/10.1016/S1359-6454(97)00027-X.
[45] D.A. Hughes, N. Hansen, D.J. Bammann, Geometrically necessary boundaries, incidental dislocation boundaries and geometrically necessary dislocations, Scr. Mater. 48 (2003) 147–153, https://doi.org/10.1016/S1359-6462(02)00358-5.
[46] X. Huang, S. Morito, N. Hansen, T. Maki, Ultrafine structure and high strength in cold-rolled martensite, Metall. Mater. Trans. A Phys. Metall. Mater. Sci. 43 (2012) 3517–3531, https://doi.org/10.1007/s11661-012-1275-5.
[47] Y.W. Liu, Z.Q. Ren, K.N. Wang, Y. Jiang, Y. Liu, J.T. Wang, Approaching the refinement limit of nano laminated structures in cubic metals by severe plastic deformation, Sci. Rep. 15 (2025) 1–19, https://doi.org/10.1038/s41598-025-92525-4.
[48] T. Yu, D.A. Hughes, N. Hansen, X. Huang, In situ observation of triple junction motion during recovery of heavily deformed aluminum, Acta Mater. 86 (2015) 269–278, https://doi.org/10.1016/j.actamat.2014.12.014.
[49] T. Yu, N. Hansen, X. Huang, Linking recovery and recrystallization through triple junction motion in aluminum cold rolled to a large strain, Acta Mater. 61 (2013) 6577–6586, https://doi.org/10.1016/j.actamat.2013.07.040.
[50] T. Yu, D.A. Hughes, Strong pinning of triple junction migration for robust high strain nanostructures, Philos. Mag. 99 (2019) 869–886, https://doi.org/10.1080/14786435.2018.1562282.
[51] A.K. Barnett, O. Hussein, M. Alghalayini, A. Hinojos, J.E. Nathaniel, D.L. Medlin, K. Hattar, B.L. Boyce, F. Abdeljawad, Triple junction segregation dominates the stability of nanocrystalline alloys, Nano Lett. 24 (2024) 9627–9634, https://doi.org/10.1021/acs.nanolett.4c02395.
[52] Y. Qin, D. Mayweg, P.Y. Tung, R. Pippan, M. Herbig, Mechanism of cementite decomposition in 100Cr6 bearing steels during high pressure torsion, Acta Mater. 201 (2020) 79–93, https://doi.org/10.1016/j.actamat.2020.09.069.
[53] S. Strodick, Scale-Bridging Micromagnetic Evaluation of Surface Integrity and Conditioning Mechanisms in Deep Hole Drilled AISI 4140 Steel, Technischen Universität Dortmund, 2024.